Structures 67 (2024) 107030

Contents lists available at ScienceDirect

Structures

journal homepage: www.elsevier.com/locate/structures

A submodeling technique for incorporating sheet metal forming effects in an AA5083 FPV structure

Sigbjørn Tveit *, Aase Reyes

Department of Built Environment, Oslo Metropolitan University, Norway

ARTICLE INFO

Keywords:
Aluminum alloy
Sheet metal forming
Submodeling
Residual stress
Fatigue

ABSTRACT

While the first generation of floating photovoltaics (FPV) was designed for operation in freshwater reservoirs, the technology is currently expanding to marine territories. In this paper, an FPV structure made from formed aluminum alloy sheets in AA5083-H111 is subject to a multi-stage numerical investigation in LS-DYNA. Quasi-static directional tensile experiments and disc-compression tests are conducted to characterize the plastic anisotropy of the rolled aluminum sheets. An anisotropic yield criterion with associated flow rule and combined isotropic-kinematic strain hardening is employed to simulate the drawing and springback of a subsection of the full structure, obtaining predictions of residual stresses, effective plastic strains, thickness change, and the process-induced geometrical imperfections. In order to analyze the performance of the formed structure under operational loads, a novel approach for submodeling that overcomes the usual requirement of precise geometric compliance enables driven variables to be obtained from a global service load model that is based on the idealized computer-aided design. The method is used to analyze geometrical, mechanical, and material-related process effects on operational stresses that are important to consider in fatigue analysis. Residual stresses were confirmed to significantly affect fatigue, while the stress increase often seen as a result of material thinning was essentially eliminated by the redistribution of internal forces. Furthermore, a parametric investigation showed that the magnitudes of the residual stresses largely depend on the alloy's kinematic hardening properties, emphasizing the importance of proper plasticity models.

1. Introduction

As the world strives toward more sustainable energy production methods, a substantial amount of research is being devoted to solving engineering problems related to novel technologies for green energy production [1]. One such technology is floating photovoltaics (FPV), which avoids the issues of land use related to traditional land-based solar farms [2]. While the first generation of FPVs was designed to operate in the hospitable environments of lakes, dams, and other freshwater reservoirs, solar technologies for use in marine territories are now emerging in the market [3]. One challenge of expanding into these environments is the increased service loads associated with waves and wind [4]. To tackle these harsh conditions, the FPV developer Sunlit Sea AS has proposed a robust design where the photovoltaics are mounted directly onto a low-profile float structure. 1.5 mm thick aluminum alloy AA5083-H111 sheets, approximately 2 × 2 m in size, are formed into a highly complex shape in a multi-step sheet metal forming (SMF) operation. Two such components are then joined together, back to back, to form a floating structural support for the panels.

In sheet metal forming, a thin metal blank is deformed into a desired geometric shape through mechanical interactions with forming tools. During the drawing operation, the material undergoes large plastic and small elastic deformations. While the plastic strains occur in a volume-preserving process that imposes thickness changes and permanent deformations, the temporary elastic strains are reversible, causing springback in the formed component upon release of the forming tools. Although the forming process can be carefully engineered to compensate for springback [5], certain deviations between the desired geometry and the obtained part are inevitable. Furthermore, spatial variations in plastic strains give rise to residual stresses in the component, as some elastic strains are restricted from returning to the stress-free state due to adjacent permanent deformations [6]. The residual stresses act as a superimposed mean stress state, while the thickness variations and the springback-induced geometric deviations influence the magnitude and distribution of stresses when the structure is subjected to external loads. Hence, understanding the SMF effects becomes particularly important

* Correspondence to: Post box 4, St. Olavs plass, NO-0130 Oslo, Norway.
E-mail address: sigbjorn.tveit@oslomet.no (S. Tveit).

https://doi.org/10.1016/j.istruc.2024.107030
Received 14 June 2023; Received in revised form 2 April 2024; Accepted 1 August 2024
Available online 8 August 2024
2352-0124/© 2024 The Authors. Published by Elsevier Ltd on behalf of Institution of Structural Engineers. This is an open access article under the CC BY license (http://creativecommons.org/licenses/by/4.0/).

for structures subjected to cyclic loading, since fatigue is known to be highly dependent on both the mean stress, and the stress amplitude [7]. For the marine FPV system, which is exposed to significant wave loads in operation, the formation of macroscopic fatigue cracks could lead to water leakage [8] or direct structural failure, compromising the service life of the product.

Much thanks to the development of Lagrangian finite element (FE) formulations for large deformation dynamic responses in the 1970′s [9] and 1980s [10], and the advancements made within phenomenological modeling of anisotropic plasticity in the 1990s and 2000s [11], it is today possible to analyze the SMF process numerically. By simulating the interaction of deformable blanks and rigid forming tools in specialized FE analysis software, predictions of final geometry, plastic strains, and residual stresses can be obtained [12,13]. Since the SMF processes are dominated by plastic deformations, the accuracy of the predictions heavily depends on the plastic constitutive relations [14–18].

The importance of accounting for such phenomena has been greatly recognized by the scientific community. This is e.g. reflected by the vast amount of research papers addressing the influence of residual stresses in the fatigue assessment of welded connections [19,20]. Yet, studies that combine SMF simulations and fatigue analyses are relatively scarce in the literature. One such investigation was conducted by Facchinetti et al. [21] who investigated the influence of SMF effects on the high-cycle fatigue (HCF) performance of a pseudo-Mac-Pherson front axle. By considering the combined effects of thinning, plastic strains, and residual stresses in the multiaxial HCF analysis framework of Dang-Van [22], they claimed to reduce safety factors by more than 15 % compared to the idealized case. However, while the importance of an accurate constitutive model for the prediction of thinning, plastic strains, and residual stresses has been highlighted in the literature, Facchinetti et al. [21] used a simple von Mises yield criterion, and a linear work hardening model where kinematic hardening effects were disregarded. In a similar study, Dannbauer et al. [23] combined sheet metal forming simulations and fatigue analysis in the investigation of a steering knuckle made of fine-grain ZStE180 sheets. They mapped sheet thinning and plastic strain results from a forming analysis in AUTOFORM to an analysis model suitable for stress analysis in Abaqus, which was used as input for fatigue analysis in FEMFAT. However, the authors did not disclose how the material plasticity was modeled, nor did they consider the effects of residual stresses. Kose & Rietman [24] implemented the results from a steering-wheel knuckle shell drawing-springback simulation, in a simplified CAD-based service load analysis, where the integration point state variables were directly transferred from the closest integration points in the forming model. The total effect of residual stresses, thinning, and plastic strains was incorporated into the analysis, leading to a reduction in the predicted fatigue damage, but the respective effects were not assessed separately. In the study, neither the fatigue model nor the plasticity formulations were accounted for, which raises uncertainties about the results.

In the review by Hariharan & Prakash [25], scenarios and challenges of integrating effects of forming in fatigue life predictions were considered. One of the challenges that were discussed relates to the adaptive mesh that is used to accurately capture the spatial variation of state variables in SMF simulations. For large complex parts, this typically results in impractically large models and high computational costs related to both the forming simulation and the fatigue analysis. Previous work combining SMF simulations and fatigue analyses has been conducted for the entire part, allowing the SMF results to be used as input for the service load analysis. This approach becomes unsuitable for the present investigation, considering the FPV structure's considerable size, the complexity of its geometry, and the multi-stage forming operation, which would result in a vast demand for storage and computational resources. To solve such issues, many commercial FE software have integrated the possibility of performing general-purpose submodeling analyses. By first conducting a simplified, full-structure analysis, a critical location can be further assessed by only examining a partition of the full geometry. In the analysis of the submodel, the software generates local boundary conditions, also referred to as driven variables, from the displacements of those nodes in the global model located on the submodel boundary. A requirement for success is geometric compatibility between the models, facilitating straightforward interpolation of the results from the global to the local nodes. In conventional shell-to-shell mapping algorithms, driven nodes are mapped to surfaces between global nodes by projection along approximated flat-surface normals [26]. The accuracy depends heavily on the projection lengths and can cause node-sequence alterations when attempting to project beyond the focal lengths of adjacent normals. Because of this, the method is inadequate for performing submodel analyses of formed structures, where the global model is generated from an idealized computer-aided design (CAD) geometry, and the submodel is a propagation of results obtained in a local SMF simulation that carries process-induced geometric imperfections.

Another issue that was raised in the review by Hariharan & Prakash [25] is the complexity of the plastic strain effect. In the studies by Kose & Rietman [24] and Dannbauer et al. [23] the influence of plastic strains on the fatigue properties was considered using the material law of steel sheets (MLSS) proposed by Masendorf [27], while Facchinetti et al. [21] used the approach of Galtier et al. [28]. After reviewing experimental reports on the influence of plastic pre-strain on the fatigue properties of the material, they concluded that the effect is dependent on the level of pre-strain, material, microstructure, load type, strain path, and geometry. To avoid presenting results based on speculative assumptions about the AA5083-H111 sheet material, the plastic strain effect is excluded from the scope of this investigation. Instead, a multi-stage numerical analysis that incorporates the SMF effects of residual stresses, local thinning, and springback-induced geometric deviations through submodeling, is performed in LS-DYNA. To reduce computational time and to gain further insights into the effects of SMF on the FPV structure's fatigue resistance, we propose a novel submodeling approach where local driven variables are obtained by interpolation with respect to normalized segment lengths along submodel boundaries. Section 2 provides a summary of the constitutive models that were employed in the numerical analysis, as well as the experimental program that was conducted to identify the model parameters for the AA5083 sheet metal. In Section 3, an overview of the formed FPV structure is given, before the three-stage submodeling analysis for incorporating sheet metal forming effects is described in detail. The results of the analysis are discussed in Section 4, where the multiaxial Sines criterion [29] is used to assess the SMF process' influence on the fatigue stresses, with special attention on the role of kinematic hardening.

2. Constitutive models and experimental calibration

In the LS-DYNA finite element simulations, the elastic behavior of the AA5083-H111 sheet is modeled as isotropic and linear. A non-quadratic anisotropic function defines the plane stress yield limit and the plastic strain increment potential through the associated flow rule. The relationship between flow stress and effective plastic strains in a proportional plastic process is described using the Voce relation [30], and the Bauschinger effect is modeled with combined isotropic-kinematic hardening. This section gives a summary of the constitutive models, as well as the experimental program that was conducted to calibrate them.

2.1. Constitutive models

When considering non-linear material behavior, the strain tensor $\boldsymbol{\varepsilon}$ is the sum of the elastic strain tensor $\boldsymbol{\varepsilon}_e$ and the plastic strain tensor $\boldsymbol{\varepsilon}_{pl}$. Assuming that the material's elastic behavior is linear and isotropic, the relationship between $\boldsymbol{\varepsilon}_e$ and the Cauchy stress tensor $\boldsymbol{\sigma}$ is given by

$$\boldsymbol{\sigma} = \boldsymbol{C}\boldsymbol{\varepsilon}_e = \boldsymbol{C}\left(\boldsymbol{\varepsilon} - \boldsymbol{\varepsilon}_{pl}\right) \tag{1}$$

where $\boldsymbol{C}$ is the fourth-rank elasticity tensor, defined in terms of the elastic modulus E and the Poisson ratio ν.

The plasticity model employs a combined isotropic-kinematic hardening law where the kinematic part is described by a backstress tensor $\boldsymbol{\alpha}$. We define the yield function f as

$$f = \widehat{\sigma} - \left(\sigma_f + B(\sigma_Y - \sigma_f)\right) \leq 0 \tag{2}$$

where the backstress-modified effective stress $\widehat{\sigma}$ is a function of the backstress-modified stress tensor $\widehat{\boldsymbol{\sigma}} = \boldsymbol{\sigma} - \boldsymbol{\alpha}$. Moreover, σ_f is the flow stress of a proportional plastic reference process, σ_Y is the stress level at the onset of yield, and $B \in [0,1]$ is the isotropic-kinematic mixing coefficient. The plastic strain-rate tensor $\dot{\boldsymbol{\varepsilon}}_{pl}$ is then expressed according to the associated flow rule as

$$\dot{\boldsymbol{\varepsilon}}_{pl} = \dot{\lambda}\frac{\partial f}{\partial \boldsymbol{s}} \tag{3}$$

where $\dot{\lambda}$ is the plastic multiplier, which is also used to calculate the evolution of the deviatoric backstress tensor $\boldsymbol{\alpha}$ [31],

$$\dot{\boldsymbol{\alpha}} = \dot{\lambda}B\frac{\frac{\partial \sigma_f}{\partial \varepsilon_{pl}}}{\frac{\partial f}{\partial \boldsymbol{s}} : \frac{\partial f}{\partial \boldsymbol{s}}}\frac{\partial f}{\partial \boldsymbol{s}} \tag{4}$$

and to define the plastic loading and elastic unloading Karush-Kuhn-Tucker condition:

$$f \leq 0; \quad \dot{\lambda} \leq 0; \quad f\dot{\lambda} = 0 \tag{5}$$

The anisotropic yield criterion by Barlat et al. [32], popularly referred to as Yld2000–2d, was employed in the numerical analyses. The criterion introduces anisotropy to the convex high-exponent Hershey-Hosford criterion [33,34] by separating the function into two parts and introducing linear transformations to the stress tensors of each part. The material model has been recognized for its ability to simulate the complex nature of plane stress plastic processes of rolled aluminum sheets [18], and is today available as a built-in material model in LS-DYNA [31]. With a being the yield function exponent, familiar from the Hershey-Hosford formulation, the Yld2000–2d function is expressed as

$$\phi = \phi' + \phi'' = 2\widehat{\sigma}^a \tag{6}$$

where the terms ϕ' and ϕ'', respectively obey the tensors $\boldsymbol{X}'$ and $\boldsymbol{X}''$. By their principle components, the two terms are written as

$$\phi' = \left|X'_1 - X'_2\right|^a \quad \phi'' = \left|2X''_2 + X''_1\right|^a + \left|2X''_1 + X''_2\right|^a \tag{7}$$

The hydrostatically independent tensors are obtained by performing linear transformations on $\widehat{\boldsymbol{\sigma}}$. For convenience, the notation $\boldsymbol{X}^{(\kappa)}$ is adopted, where the superscript κ represents the different transformed tensors. Establishing a coordinate system xyz, where the respective axes are aligned with the sheet's rolling direction (RD), transverse direction (TD), and normal direction (ND), the transformed tensors can be expressed as

$$\boldsymbol{X}^{(\kappa)} = \boldsymbol{L}^{(\kappa)}\widehat{\boldsymbol{\sigma}} = \begin{bmatrix} L_{11}^{(\kappa)} & L_{12}^{(\kappa)} & 0 \\ L_{21}^{(\kappa)} & L_{22}^{(\kappa)} & 0 \\ 0 & 0 & L_{44}^{(\kappa)} \end{bmatrix} \begin{bmatrix} \widehat{\sigma}_{xx} \\ \widehat{\sigma}_{yy} \\ \widehat{\sigma}_{xy} \end{bmatrix} \tag{8}$$

The components of the transformation tensors $\boldsymbol{L}'$ and $\boldsymbol{L}''$ are taken as

$$\begin{Bmatrix} L'_{11} \\ L'_{12} \\ L'_{21} \\ L'_{22} \\ L'_{44} \end{Bmatrix} = \begin{bmatrix} -2/3 & -0/0 & -0/0 \\ -1/3 & -0/0 & -0/0 \\ -0/0 & -1/3 & -0/0 \\ -0/0 & -2/3 & -0/0 \\ -0/0 & -0/0 & -0/1 \end{bmatrix} \begin{Bmatrix} \alpha_1 \\ \alpha_2 \\ \alpha_7 \end{Bmatrix};$$
$$\begin{Bmatrix} L''_{11} \\ L''_{12} \\ L''_{21} \\ L''_{22} \\ L''_{44} \end{Bmatrix} = \frac{1}{9}\begin{bmatrix} -2 & -2 & -8 & -2 & -0 \\ -1 & -4 & -4 & -4 & -0 \\ -4 & -4 & -4 & -1 & -0 \\ -2 & -8 & -2 & -2 & -0 \\ -0 & -0 & -0 & -0 & -9 \end{bmatrix} \begin{Bmatrix} \alpha_3 \\ \alpha_4 \\ \alpha_5 \\ \alpha_6 \\ \alpha_8 \end{Bmatrix} \tag{9}$$

where α_1 to α_8 are the model's anisotropy coefficients. When all anisotropy coefficients are unity, the model reduces to the isotropic Hershey-Hosford formulation, which further reduces to the von Mises criterion when the exponent $a = 2$ or 4, and the Tresca criterion when $a = 1$ or ∞. The exponent dictates the yield locus' radii, and it is commonly accepted that $a = 6$ and 8 give good representations of BCC and FCC materials [34], respectively.

The material's plastic work hardening was modeled using the Voce relation [30], which defines the flow stress, and the stress at the onset of yield

$$\sigma_f(\varepsilon_{pl}) = K - L\exp(-M\varepsilon_{pl}) \tag{10a}$$

$$\sigma_f(\varepsilon_{pl} = 0) = \sigma_Y = K - L \tag{10b}$$

where K, L, and M are the Voce parameters, and ε_{pl} is the equivalent plastic strain in a proportional plastic process.

2.2. Uniaxial tensile tests

To calibrate the anisotropic yield criterion, uniaxial tensile tests were performed at different angles θ to the sheet's rolling direction, characterizing the directional dependencies of the material's plastic behavior. While the plane stress Yld2000–2d yield criterion can be calibrated to uniaxial tensile test data from tension in three different directions in the plane of the sheet, full stress (3D) models such as Yld2004–13/18p [35] and Yld2011–18/27p [36] depend on calibration to data from seven different directions. To avoid constraining the scope of future investigations that rely on the full stress state, the experimental program included tests at θ = 0°, 15°, 30°, 45°, 60°, 75°, and 90°. Several parallels were conducted for each test: five in the reference direction, and three in the other directions.

The SIMLab UT200 specimen, displayed in Fig. 1(b), was adopted for the experimental study. The specimen geometry has been extensively used for plasticity characterization of metal sheets and plates (e.g. [37–41]). The specimens were produced by waterjet cutting with a tolerance of ± 0.1 mm. To reduce the uncertainties related to the geometric precision of the rolling and waterjet cutting, width and thickness measurements were performed with caliper and screw gauge at three locations along the specimen shaft (cf. Fig. 1(b)), and the arithmetic means were used to calculate the initial cross-section area A_0.

Quasi-static uniaxial tensile tests were performed in a Galdabini Quasar 250 machine, with a crosshead velocity of 4 mm/min, corresponding to a strain rate of approximately 10^{-3} s^{-1} prior to necking. A LaVision digital image correlation (DIC) system [42] was used to measure the in-plane strain fields. The specimens were given a base coat of white aerosol spray paint before an airbrush was used to apply a finely grained pattern of black speckles. A setup of two high-resolution digital cameras and two flashes (see Fig. 1(a)) was directed at the speckled test

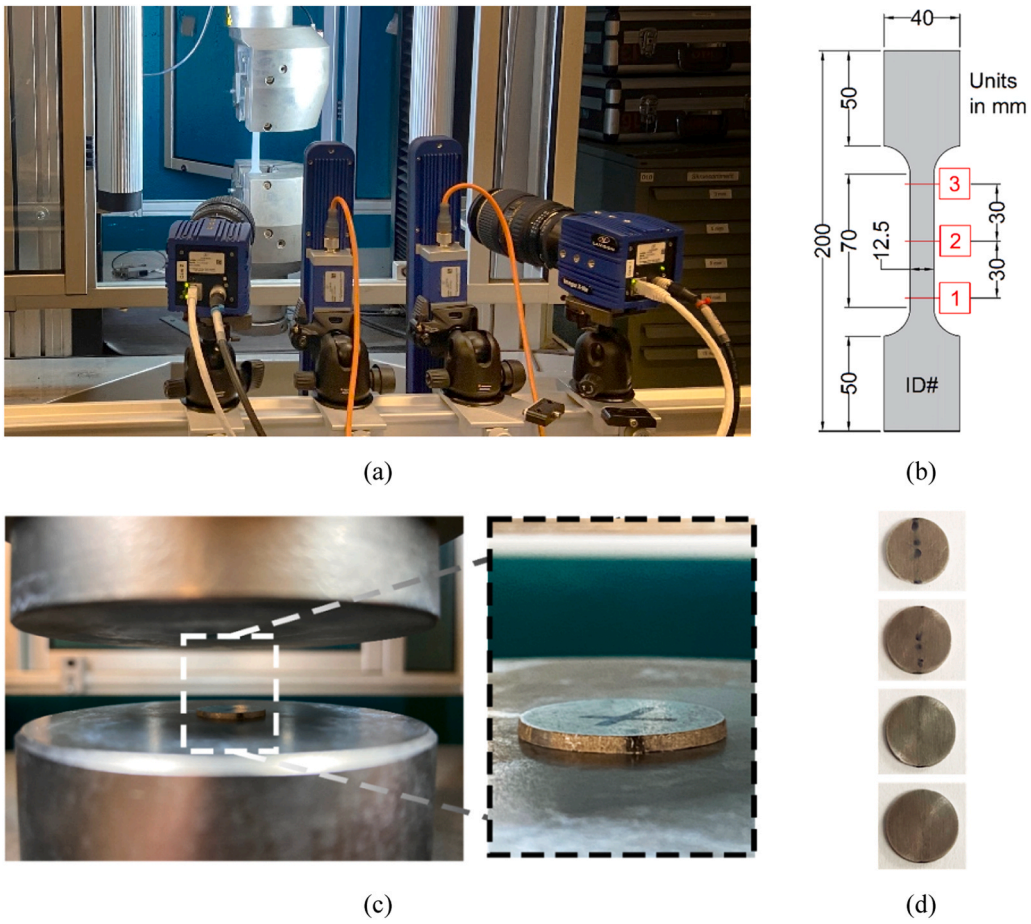

Fig. 1. Experimental tests. (a) DIC setup. (b) Geometry of uniaxial test specimen. Units in mm. (c) Through-thickness disc compression test setup. (d) Disc specimen subject to successive compressions. From top to bottom: undeformed, compression force of 41.0 kN, 65.1 kN, and 75.4 kN.

specimens from a distance of approximately 0.8 m and synchronized with the test machine. The stereo angle between the two cameras enables the DIC system to trace the displacements of the speckled surface within a three-dimensional calibrated volume, allowing the user to establish virtual strain gauges to measure engineering strains in the specimen's length and width directions, $e_l = \Delta L/L_0$ and $e_w = \Delta W/W_0$, where subscript zero represents initial gauge lengths, and the delta notations represent the change of gauge lengths. The corresponding logarithmic strains were calculated as $\varepsilon_l = \ln(1+e_l)$, and $\varepsilon_w = \ln(1+e_w)$, and the thickness strain was taken as $\varepsilon_t = -(\varepsilon_l+\varepsilon_w)$, by the assumption of volume-preserving plastic processes. The engineering stress $s = F/A_0$, where F is the measured force, was used to compute the true stress as $\sigma = s(1+e_l)$. The plastic strain was then calculated as $\varepsilon_{pl} = \varepsilon_l - \sigma/E_{sys}$, where E_{sys} is the measured tensile test system stiffness, which was determined from the linear part of the measured stress-strain diagram.

2.3. Through thickness disk compression (TTDC) tests

Upon uniaxial compression in the through-thickness direction of a thin disc, the specimen yields a state that is equivalent to equibiaxial tension in terms of deviatoric stresses [32]. In the TTDC test, this is utilized to experimentally measure the equibiaxial strain ratio $R_b = d\varepsilon_{TD}/d\varepsilon_{RD}$ of an anisotropic sheet material. Circular discs were exerted to a compressive force large enough to cause plastic deformations. The disc specimens had an initial diameter $D_0 = 12.7$ mm to comply with the original study where the test method was proposed [32], and several subsequent investigations (e.g. [43–45]). The tests were performed in the same Galdabini Quasar 250 test machine, now equipped with self-aligning hardened steel plates (see Fig. 1(c)). Six parallels were conducted to rule out inconsistencies, and each disc was successively subjected to three different levels of compression (see Fig. 1(d)). Prior to each cycle, PTFE-based dry film aerosol lubricant was applied to all faces of contact. The diameters in RD and TD were measured in the undeformed state and after each compression, using a 10 μm precision screw gauge. The directional true strains were calculated from the initial diameter D_0, and the deformed diameter D, as $\varepsilon_{RD} = \ln(D_{RD}/D_{0,RD})$ and $\varepsilon_{TD} = \ln(D_{TD}/D_{0,TD})$.

2.4. Material test results

A collection of representative engineering stress-strain curves from different orientations is displayed in Fig. 2(a). The curves follow the same trend, displaying moderate anisotropy in flow stress, and a pronounced Portevin-Le Chatelier (PLC) effect [46], characterized by serrated plastic flow (see close-up in Fig. 2(b)). The effect has been described for AA5083 in existing literature [47–50] and falls outside the present scope. Flow stress ratios $r_\theta = \sigma_\theta/\sigma_0$ were obtained at the specific plastic work $W_{pl} = \int_0^{\varepsilon_{pl}} \sigma d\varepsilon_{pl} = 25$ MPa, and transverse strain ratios $R_\theta = d\varepsilon_w/d\varepsilon_t$ were taken as the slopes of linear regressions to the width and thickness strain curves (see Fig. 2(c)). The seven UT tests constituted 14 data points that were all included in the calibration dataset for obtaining the Yld2000–2d anisotropy coefficients. The disc compression tests provided yet another data point, namely the equibiaxial strain ratio $R_b = d\varepsilon_{TD}/d\varepsilon_{RD}$, which was calculated from the slope of a linear regression to the strains in TD and RD, measured at different levels of permanent through-thickness deformation (cf. Fig. 2(d)). The last data point of the calibration set, the equibiaxial stress ratio $r_b = \sigma_b/\sigma_0$, was taken as the

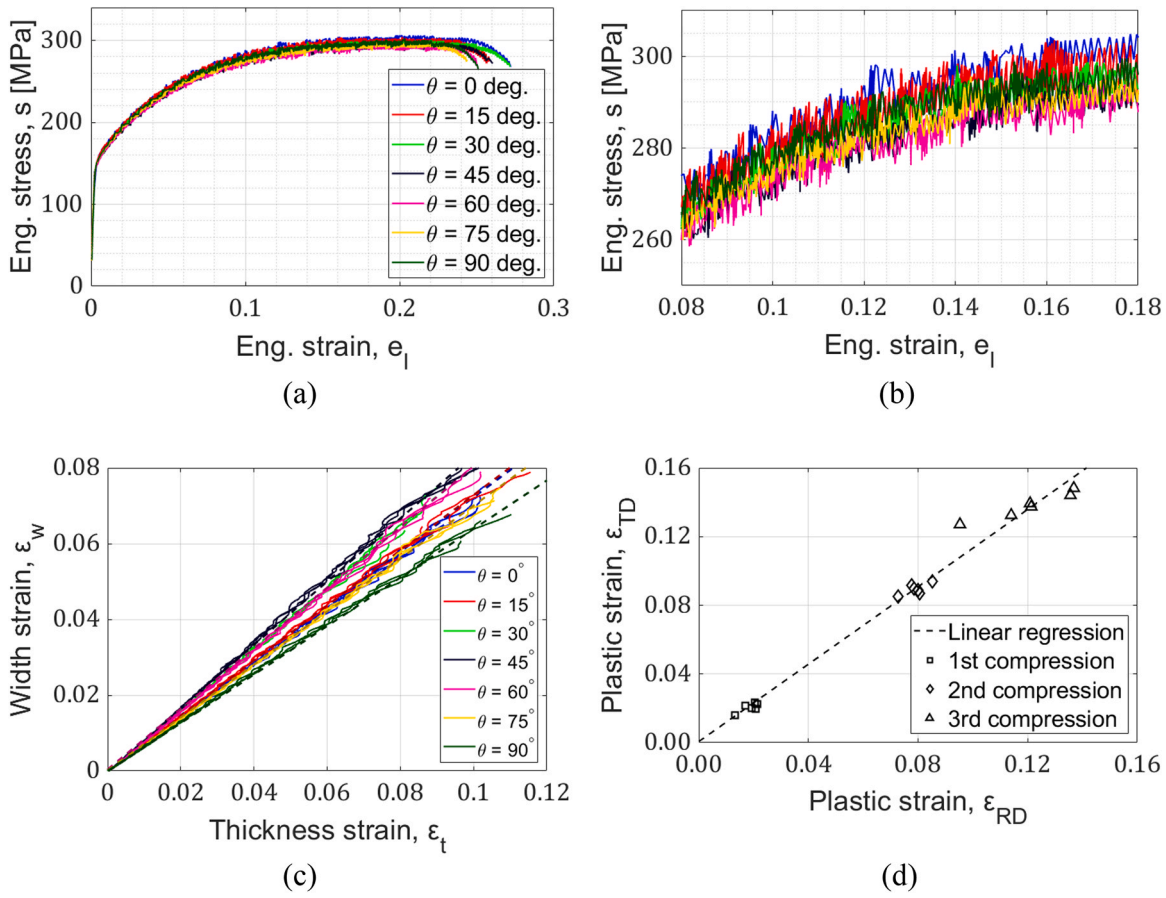

Fig. 2. Material test results. (a) Engineering stress-strain curve; (b) Close-up of PLC serrations; (c) Width vs. thickness strains from UT tests and associated linear regressions (dashed). (d) Plastic strain in TD vs. RD from TTDC tests, and linear regressions (dashed).

Table 1
Experimental anisotropic plasticity parameters for AA5083-H111.

Plastic strain ratios	R_0	0.7142
	R_{15}	0.7284
	R_{30}	0.8025
	R_{45}	0.8357
	R_{60}	0.7998
	R_{75}	0.6991
	R_{90}	0.6410
	R_b	1.1263
Flow stress ratios	r_0	1.000
	r_{15}	0.9919
	r_{30}	0.9819
	r_{45}	0.9752
	r_{60}	0.9737
	r_{75}	0.9811
	r_{90}	0.9908
	r_b	1.000*

* Assumed isotropic upon lack of experimental bulge test data.

Table 2
Model parameters for AA5083-H111.

Elastic parameters	Young's modulus, E (MPa)	72 000
	Poisson's ratio, ν	0.33
	Density, ρ (kg/m^3)	2650
Voce relation	K (MPa)	379.85
	L (MPa)	228.73
	M	13.383
Yld2000 −2d yield criterion	α_1	0.9602
	α_2	0.9836
	α_3	0.9724
	α_4	1.0219
	α_5	1.0076
	α_6	0.9592
	α_7	1.0078
	α_8	1.0869
	α	8

isotropic value of unity upon lack of experimental bulge test data. The measured anisotropic plasticity parameters are summarized in Table 1, while the calibrated model parameters are given in Table 2.

The calibration was performed in a minimized sum of squared errors-procedure, using the quasi-Newton algorithm of *fminunc* in MATLAB [51]. The ability of the Yld2000–2d criterion to accurately capture the measured behavior seen in the extended experimental data set is demonstrated in Fig. 3(a)-(b), while the yield loci contour plot is displayed in Fig. 3(c). The three Voce parameters were fitted in a similar manner to the data of true stress σ and plastic strain ε_{pl}, from the five parallels at $\theta = 0°$, where the onset of necking at maximum engineering stress was used as the upper cut-off limit for the calibration data. From the obtained parameters (reported in Table 2), the measured stress at the onset of yield was determined as $\sigma_Y = K - L = 151.12$ MPa. The fitted Voce curve is presented in Fig. 3(d) along with the measured data, displaying limited scatter between parallel tests.

3. Numerical structural analysis

3.1. Background

In the FPV solution developed by Sunlit Sea AS, the PV panel is mounted directly onto a buoyant structure composed of two identical

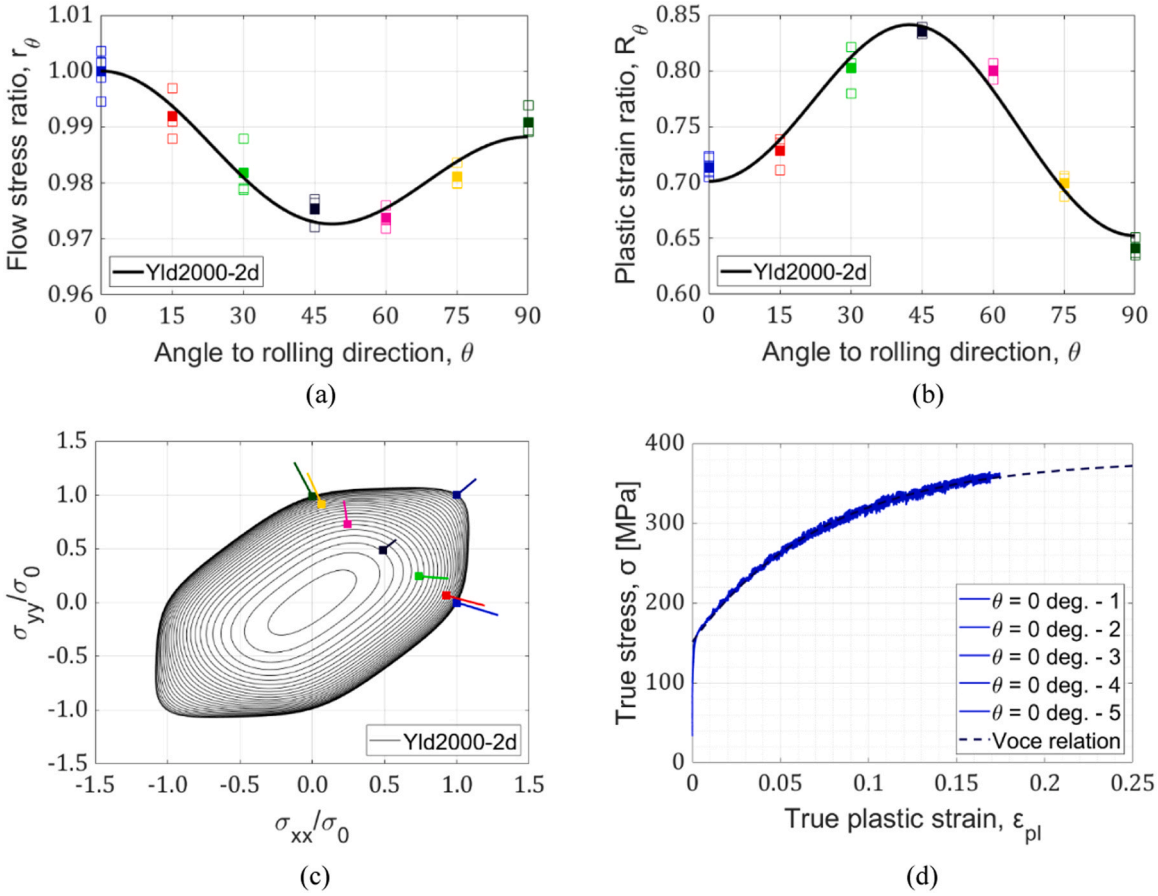

Fig. 3. Calibrated plasticity models. Measured and predicted (a) flow stress ratios and (b) plastic strain ratios. (c) Yld2000–2d loci contours at constant magnitudes of shear stress σ_{xy}. (d) Experimental true stress vs. plastic strain curves and fitted Voce relation. Hollow squares indicate parallels and filled squares indicate average measurements.

aluminum sheet components that are joined together and sealed off along the edges. The components are produced by a two-stage forming operation where 1.5 mm thick rolled AA5083-H111 sheets are deep-drawn into a cupcake-tray-like shape. The float provides a stable platform in harsh weather conditions, capable of supporting the weight of maintenance personnel and equipment, while it acts as a thermal bridge between the photovoltaic panels and the cool seawater, enhancing the efficiency of each unit. The FPV unit assembly and the formed aluminum component are depicted in Fig. 4(a).

The FPV plant can be scaled to meet a desired energy production capacity by organizing the units into a matrix, where the units are reciprocally connected with two polyurethane hinges on every edge of the square units. The matrix is stabilized by a surface mooring system (see Fig. 4(b)), which applies tension to the perimeter of the matrix, preventing the panels from colliding under the operational metocean condition. The lines of the surface mooring are connected to four buoys that are maintained in a global position by the station-keeping of a site-specific subsurface mooring system, which can take different forms depending on the operational environment.

The operational internal stresses of the FPV structure arise from an extended set of phenomena related to the manufacturing process and the operational conditions. In addition to the sheet metal forming process,

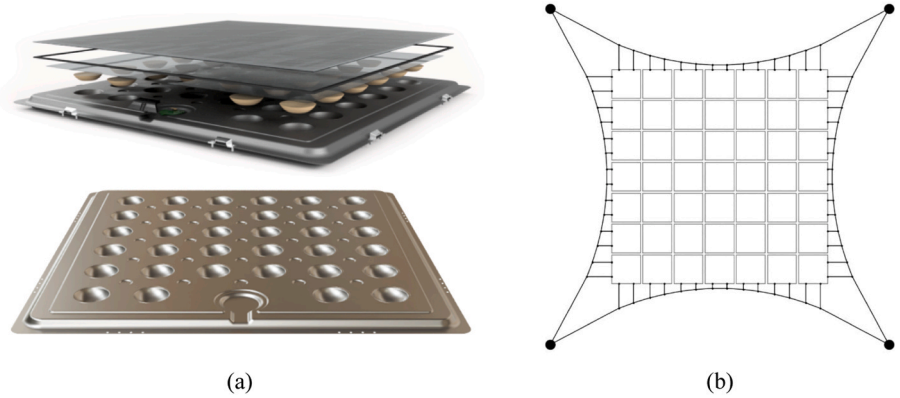

Fig. 4. Floating photovoltaic system. (a) Float assembly and AA5083 component. (b) Sketch of FPV matrix, and mooring system for a 25 kWp system. Reprinted with permission from Sunlit Sea AS.

the method that is used to join the two components (e.g. welding or clinching) may alone influence the stress fields. Moreover, the complex fluid-structure interaction between the moored system of FPV units and the waves and currents of the marine environment, alone deserves a dedicated investigation. The work presented in this article is not an attempt at performing a comprehensive structural analysis of Sunlit Sea's FPV system. Instead, we aim to establish a framework for analyzing the sheet metal forming process' effects on the structure's operational stresses. In the current application of the methodology, we limit ourselves to considering the sheet metal forming effects in combination with a simplified load case that models wave loads and mooring tension. Thus, in this study, the contributions to the operational stresses can be classified as (a) stresses due to wave loads, (b) stresses due to mooring tension, and (c) residual stresses that arise from the sheet metal forming.

In Section 3.2, we conduct global analyses of the structure, by exerting forces to the FPV structure at the connector locations. A critical location is identified, and an in-plane area of 420 × 520 mm surrounding this location is taken as a submodel for further investigation. In Section 3.3, the metal sheet forming process of the submodel region is simulated in LS-DYNA. An undeformed blank, that initially measures 437 × 520 mm, is deformed in a forming-springback simulation to obtain post-forming displacements, strains, and stresses in the 420 × 520 mm output model. The calibrated anisotropic plasticity models from Section 2 are implemented in a forming-springback simulation to obtain the post-manufacturing residual stresses of category (c). In Section 3.4, a quasi-superposition submodel analysis is performed, where service load cases are constructed from the global analyses by superposition, to represent the structural response to wave loads and mooring tension. The translational and rotational displacements at the submodel boundary are transferred to the sheet metal forming model by a mapping technique based on normalized segment length interpolation.

3.2. Global service load analysis

For the global linear FE model, CAD geometry provided by the FPV manufacturer was used to generate a mesh of fully integrated shell elements, with seven through-thickness integration points for a static implicit analysis in LS-DYNA. The problem was reduced by applying symmetry constraints along the rim of the structure, and in the center of each cup, where the two components are joined together.

To assess the structure's response to loads applied at the hinge connectors, loads in the global X and Y direction (respectively referred to as mode I and II loading) were applied to the statically determinate structure (c.f. Fig. 5(a)). A force P, which is used as a unit force in further analysis, was established as 90 % of the connector force required to introduce plastic strains upon application of equal tension in both directions, simultaneously. The two modes and the reference force P allowed the generation of arbitrary load combinations through scaling and superposition.

By examining the near-surface stress fields, a high-stress region was identified at the inlet of the float's electrical compartment. An in-plane area of 420 × 520 mm around this location was taken as a submodel for further investigation, and the region was iteratively updated with a refined mesh, as displayed in Fig. 5(b). The maximum von Mises stress from the two near-surface integration points for Mode I + Mode II loading is exhibited in Fig. 5(c) for the model with the refined mesh.

3.3. Local forming analysis

To incorporate the effects of manufacturing on in-service stresses, a finite element simulation of the aluminum sheet forming process of the submodel domain was performed in LS-DYNA, where the calibrated material models from Section 2 were implemented. Symmetry constraints were applied at the boundaries along the north, west, and south segments (cf. Fig. 5(b)). Forming tool geometries were taken from a CAD model of the full sheet metal forming press, provided by the FPV manufacturer. A stationary die, two blank holders, and four other forming tools were modeled as rigid shells (see Fig. 6(a)), with individually prescribed velocity histories, and a frictionless one-way surface-to-surface contact rule governing the interaction between the forming tools and the blank. The blank was modeled with reduced integration Belytschko-Tsay elements with seven through-thickness integration points [52] with an initial element size of approximately 6.7 mm. To ensure appropriate spatial discretization while limiting computational cost, a four-level adaptive meshing algorithm was employed, triggering h-refinements upon the approach of contact surfaces, or whenever the total rotation relative to surrounding elements

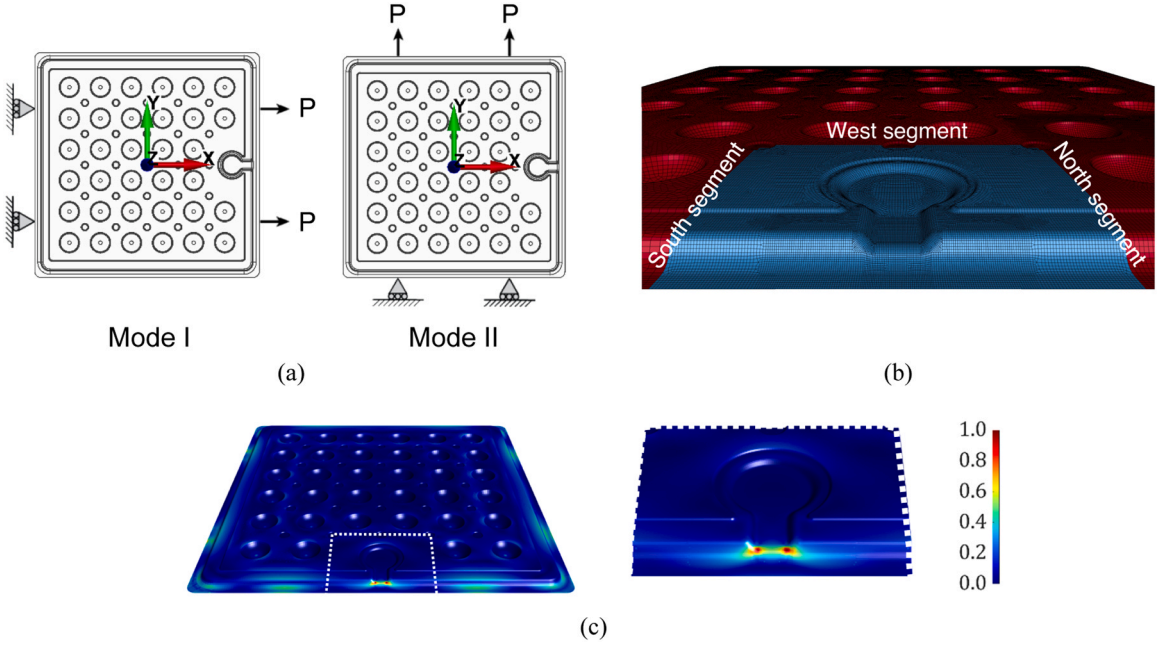

Fig. 5. Global analysis model. (a) Forces in global X (mode I) and Y direction (mode II). (b) Refined submodel as part of the global analysis model. (c) Normalized von Mises maximum surface stresses from global analysis (Mode I + Mode II).

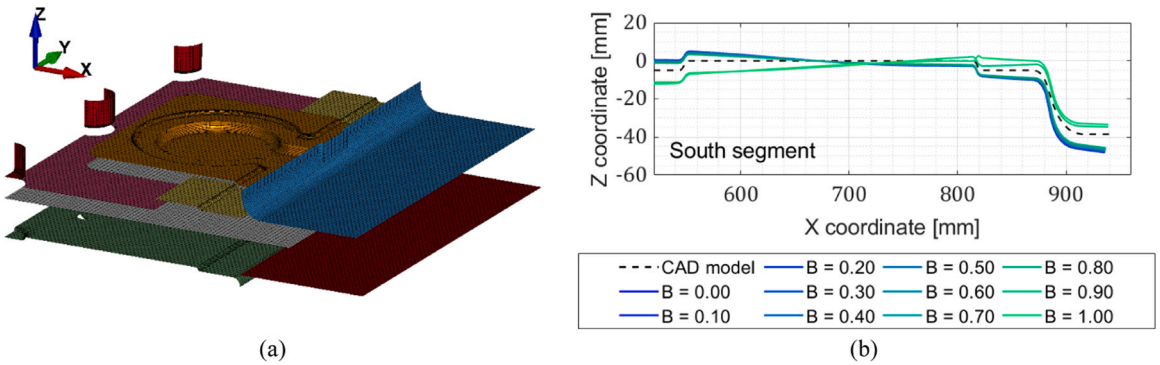

(a) (b)

Fig. 6. Local forming simulation. (a) Assembly of forming tools, and deformable blank (grey). Distances between parts are exaggerated for illustrative purposes. (b) Comparison between submodel boundary segment profiles: Idealized CAD geometry (global model), and local forming model predictions with different mixing coefficients B.

exceeded a threshold of five degrees per level. Moderate selective mass scaling was used to speed up the central difference explicit time-integration without inducing significant dynamic effects. The blank, which in the undeformed state measured 437 × 520 mm, contracted 17 mm along the west-east direction during drawing, resulting in an in-plane area of 420 × 520 mm, corresponding to the submodel region established in Section 3.2.

Following the dynamic drawing step, the elastic springback was simulated in a static analysis. Only a rigid body motion constraint in the global Z direction was applied, in addition to the propagated symmetry constraints. For this analysis, high-accuracy fully integrated shell elements (ELFORM −16) were used. Eleven different drawing-springback scenarios were simulated, with the isotropic-kinematic mixing coefficient B varying from $B = 0.0$ (isotropic) to $B = 1.0$ (kinematic). Fig. 6(b) displays the predicted profile of the south boundary segment for the different values of B, next to the idealized CAD geometry of the global model.

3.4. Local service load analysis

For the local service load analysis, a submodel was established from the results of the local forming simulations. From the *dynain* output files from the LS-DYNA forming analyses, models that contained the spatial configuration of nodes and elements, shell thicknesses, stress tensors (Cauchy and backstress), effective plastic strains, and nodal boundary conditions from the preceding simulations, were created. Nodal results from the global and local models were read from ASCII files. Submodel boundary segment lengths were then calculated for each model as the sum of Euclidian norms between neighboring nodes along the boundaries, normalized by the respective total segment lengths. This variable was used as a parameter for geometric mapping between equivalent locations in the global and the local models, which allowed interpolation of six degrees-of-freedom (DOF) nodal displacements, using a not-a-knot end condition cubic spline in MATLAB [51]. The propagated boundary conditions were then deleted from the local *dynain* output files and replaced with the driven variables obtained from the interpolation. Fig. 7 displays the variation of the nodal DOFs in the global model with respect to the normalized segment length interpolation variable.

Assuming that the submodel boundary displacements remain linear in the presence of forming-induced stresses and strains allows analyzing different load cases by scaling and combining mode I and II boundary displacements. In this investigation, we chose to explore a load cycle consisting of constant mooring tension with alternating wave loads in the global X direction. Results from the global modes I and II were scaled to obtain an equal tension mean force in all eight connectors of $P_{X,m} = P_{Y,m} = 0.5P$, and the wave load cycle was modeled by scaling the global

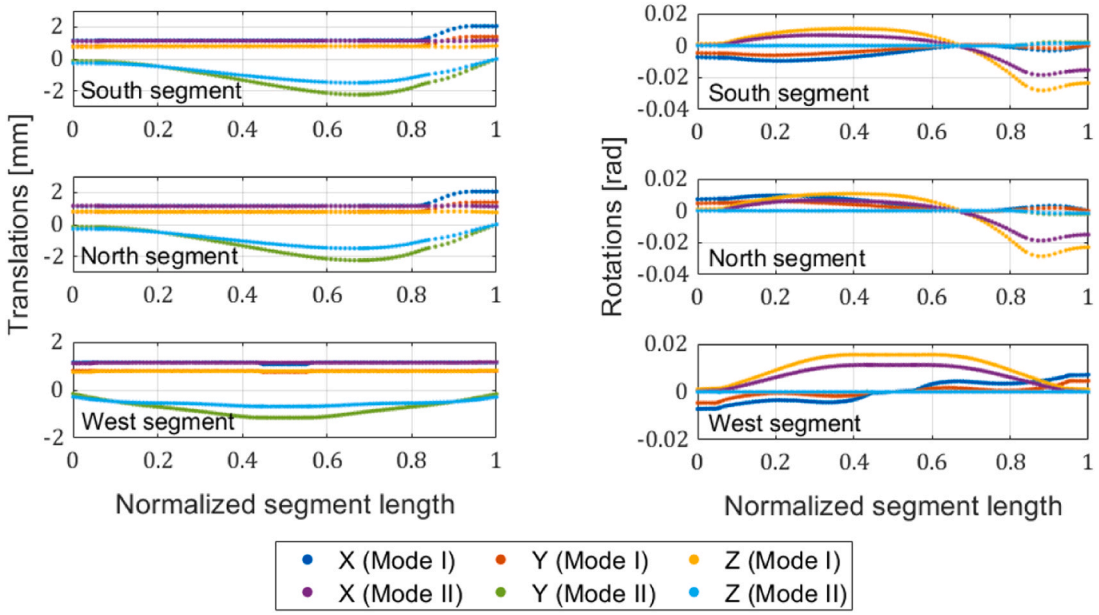

Fig. 7. Global analysis results: Nodal displacements at the submodel boundaries for the two deformation modes.

mode I to obtain the alternating component $P_{X,a} = 0.3P$. Carrying the geometry, thinning, plastic strains, and residual stresses from the post-springback configuration, the mean state ($P_X = 0.5P$ and $P_Y = 0.5P$) and the maximum state ($P_X = 0.8P$ and $P_Y = 0.5P$) were run as static analyses in LS-DYNA. From these two instances, the load cycle's mean and amplitude stress tensors could be constructed in MATLAB from stress tensor data written to ASCII files.

4. Results and discussion

With the introduction of sheet metal forming effects, the structure's stress configuration is severely changed compared to predictions made with the idealized global model. The differences arise from several sources and may be classified as geometric, mechanical, and material effects. Even with carefully designed SMF processes, formed components will typically deviate from the intended geometry. Phenomena such as springback and local buckling may increase, reduce, or introduce new radii and curvatures to the manufactured component, as well as the simulation model. To study the influence of geometric deviations, a stripped reference model that carried only the geometric configuration obtained from the SMF simulation was established by removing residual stresses, effective plastic strains, and shell thickness variations from the *dynain* output file. Comparing the results obtained with the global analysis model allows studying the combined influence of two different effects. The first effect is synthetic and arises from the misalignments between submodel boundaries of the idealized global model, and the formed local model (cf. Fig. 6(b)). As displayed in Fig. 8(a), this causes local, non-physical stress concentrations near the submodel boundary. The derivative of the global Z-coordinate with respect to the interpolation variable is plotted in Fig. 8(b) for the south boundary segment. The effect is pronounced where the

difference in slope between the formed ($B = 0.5$), and the idealized geometry is large. Although the hot spots rapidly vanish when moving away from the boundary, an abundant distance to the region of interest is preferable to ensure that the results in the region of interest are not contaminated. The second effect is physical and relates to the difference between the stress distributions in the formed component and the idealized model. The local forming analysis predicts the occurrence of local buckling near the critical location, which when subjected to service loads causes internal forces to channelize. Hence, at the critical location, the stripped reference model obtained from forming displayed surface von Mises stresses of 113.6 MPa at the peak load case ($P_X = 0.8P$, and $P_Y = 0.5P$), as opposed to the 101.1 MPa that were obtained when running the same load case with the CAD-based global model.

Another phenomenon that falls within the category of geometric effects is sheet thinning, which was investigated by re-adding the predicted shell thicknesses to the stripped reference model. Previous studies have reported significantly altered stress magnitudes upon including plastic strain-induced thickness variations (e.g. [21,53]). Despite a variation in thickness from 1.22 mm (−19.2 %) to 1.67 mm (+10.6 %) for $B = 0.5$, the influence on surface stress was minor in our study. When examining the structure subjected to the load cycle maximum, only smaller differences were observed among individual stress tensor components, and the von Mises stress fields were virtually uninfluenced. The major local moments and normal forces were reduced by 56.8 % and 10.6 % at the location of minimum thickness, and increased by 22.7 % and 7.7 % at the location of maximum thickness. This suggests that any change in stress per unit force due to through-thickness plastic strains were almost eliminated by the redistribution of internal forces according to the stiffness variation of the formed component. This apparent contradiction with findings reported by other authors is likely due to the locality of the thickness variations in the current model, which enables efficient redistribution.

It is well-known that the presence of tensile mean stresses negatively affects the fatigue life. Mean stresses and stress amplitudes are treated differently in various existing multiaxial high-cycle fatigue (HCF) criteria, but a popular choice in orientation-invariant formulations is to assume that the stress amplitude contributes to the effective fatigue stress through the von Mises stress $\sigma_{VM,a}$, and the mean stress through the first stress tensor invariant $I_{1,m}$ [54–56]. The residual stresses from the forming operation superimpose a constant stress state that acts along with any other operational loads. Adopting the mean stress dependency of AA5083 from [57,58], $A = 0.185$, and the multiaxial Sines criterion [54], the effective fatigue stress S can be written as a sum of contributions from service loads, and SMF-induced residual stresses, $S = S_{service} + S_{RS}$, where

$$S_{service} = \sigma_{VM,a,wave} + 0.185 I_{1,m,moor} \tag{11}$$

$$S_{RS} = 0.185 I_{1,m,RS} \tag{12}$$

A fringe plot of the surface Sines stresses for the load case in Section 3.4 based on the model with mixing coefficient $B = 0.5$ is given in Fig. 9 (a). The stacked bar plot in Fig. 9(b) presents the maximum predicted surface Sines stress of each analysis with varying B, exhibiting a complex non-linear dependency. The analyses with $B \leq 0.4$ share approximately the same critical location on the structure's bottom surface, exhibiting a negative correlation between increased kinematic hardening and the maximum Sines stress S. In this domain, the contribution by residual stresses ranges from 41.2 to 54.5 %. A slight negative correlation continues for $B \geq 0.5$, however the critical location shifts to a nearby position, on the structure's top surface about 10 mm away, where the total fatigue stress intensity is heavily dominated by contributions from residual stresses (from 73.3 to 94.3 %). Compared to the predictions of the CAD-based global model, indicated by the dashed line in Fig. 9(b), the maximum Sines fatigue stress was respectively increased by factors of 2.75 and 1.61 in the isotropic ($B = 0.0$) and kinematic ($B = 1.0$) formulations. When interpreting these results, it is worth noting that the linear mean stress dependency adopted from [58] is obtained from experimental fatigue limits [57] of cyclic stress where $\sigma_{\max}/\sigma_{\min} = 0.1$ and 0.5, which implies a significant extrapolation for the cases $B \geq 0.6$,

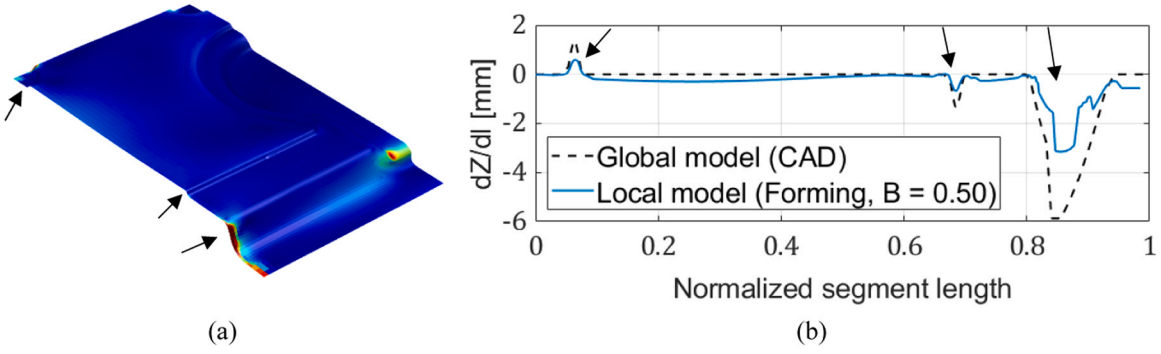

Fig. 8. Non-physical stress concentrations caused by boundary misalignments. (a) Boundary hot spots (arrows). (b) Slopes of south segments.

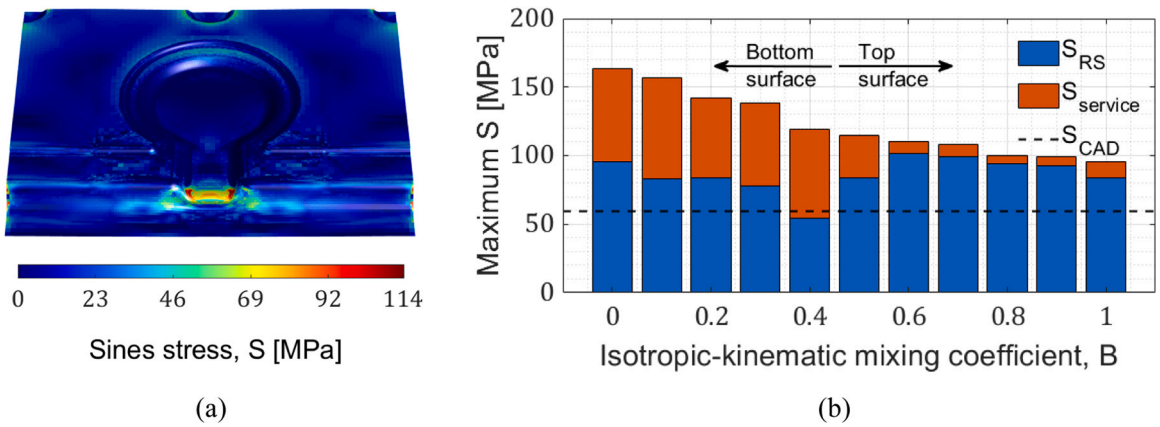

Fig. 9. Surface Sines stress. (a) Fringe plot ($B = 0.5$). (b) Maximum surface Sines stress evaluated for different values of B and compared to predictions from the CAD-based global model (dashed line).

that is prone to be non-conservative. Another notable remark concerns the stress-based HCF criterion's limited propriety to linear elastic stress amplitudes. The presented results employ amplitude terms (cf. Eq. (11)) calculated from the positive part of the load cycle. While the assessed load case produced linear elastic behavior in the idealized global model, local material non-linearities were seen in the models where SMF effects were incorporated. Because SMF imposes various stress paths and magnitudes of plastic strains in different locations, the manufactured component is left in a complicated state with spatially varying mechanical properties. Furthermore, the special case of pure isotropic hardening leaves an elastic domain that is artificially large, while the pure kinematic formulation results in a confined elastic domain that upon further loading could predict premature plastic deformations. Moreover, upon introducing non-isotropic hardening formulations, the elastic limit of successive stress paths will depend on their proportionality with the backstress tensor. This means that predicting whether or not an operational stress state is within the material's elastic limit becomes a non-trivial task that relies on the accuracy of the hardening law, the yield surface and the flow rule, and the modeling of any other plasticity-related phenomena, such as the PLC effect. It also suggests that a dedicated assessment of fatigue performance may call for models that treat high-cycle and low-cycle fatigue (LCF) in a unified manner.

5. Conclusion

This paper presents a comprehensive numerical analysis of the effects of sheet metal forming on the operational stresses of an aluminum sheet floating photovoltaic structure. Material tests of rolled sheets in AA5083-H111 were conducted to calibrate a non-linear hardening law and an anisotropic yield criterion. The calibrated plasticity model was implemented in a three-stage numerical analysis in LS-DYNA that combined local sheet metal forming simulations with submodeling in a novel manner. The problems with geometric incompatibility that are encountered in conventional shell-to-shell mapping procedures were overcome by interpolating the nodal DOFs with respect to normalized submodel boundary segment lengths. The model was used to study various SMF-induced effects, with particular emphasis on aspects that influence fatigue, leading to the following key conclusions:

- Effects related to geometric differences between the simulated model and the CAD-based model alone represented a significant increase in the maximum von Mises surface stress of 12.4 %.
- Sheet thickness change ranged from −19.2 to 10.6 % (for the kinematic coefficient $B = 0.5$) in local regions, but the change in stress that often follows thickness change was essentially eliminated due to redistribution of internal forces.
- The maximum Sines surface stress was substantially increased when including the combined effects of SMF. The increase ranged monotonically from a factor of 2.75 in the purely isotropic case ($B = 0.0$), to 1.61 in the purely kinematic case ($B = 1.0$). A bifurcation occurred when $0.4 > B > 0.5$, where the maximum moved from a location on the inner surface to a nearby location on the outer surface that was almost entirely dominated by the contributions of SMF-induced residual stresses.

Further research is advised to concern experimental validation of the SMF simulations, and identification and modeling of the material's combined isotropic-kinematic hardening behavior. A dedicated fatigue life assessment could be expanded to include in- and out-of-phase multidirectional load cases of realistic sea states, employing fatigue limit criteria that can handle arbitrary multiaxial stress histories, while treating high-cycle and low-cycle fatigue in a unified manner. This would also require experimental evidence of how plastic strains influence the fatigue strength of AA5083-H111.

CRediT authorship contribution statement

Aase Reyes: Conceptualization, Funding acquisition, Methodology, Project administration, Resources, Supervision, Validation, Writing – review & editing. **Sigbjørn Tveit:** Conceptualization, Data curation, Formal analysis, Funding acquisition, Investigation, Methodology, Project administration, Resources, Software, Validation, Visualization, Writing – original draft, Writing – review & editing.

Declaration of Generative AI and AI-assisted technologies in the writing process

During the preparation of this work, the authors used Chat GPT to improve the readability and language of selected paragraphs. After using this tool/service, the authors have reviewed and edited the content as needed, and take full responsibility for the content of the publication.

Declaration of Competing Interest

The authors declare that they have no known competing financial interests or personal relationships that could have appeared to influence the work reported in this paper.

Acknowledgements

The present work was carried out with financial support from the Faculty of Technology, Arts and Design, Oslo Metropolitan University. The authors would like to acknowledge Rune Orderløkken and Paban

Acharya for assistance with the experimental program, and Sunlit Sea AS for providing test specimens, geometry files, and information necessary to conduct the investigation.

References

[1] Tan H, Li J, He M, Li J, Zhi D, Qin F, et al. Global evolution of research on green energy and environmental technologies: A bibliometric study. J Environ Manag 2021;297:113382. https://doi.org/10.1016/j.jenvman.2021.113382.

[2] Essak L, Ghosh A. Floating photovoltaics: a review. Clean Tech 2022;4:752–69. https://doi.org/10.3390/cleantechnol4030046.

[3] Vo TTE, Ko H, Huh J, Park N. Overview of possibilities of solar floating photovoltaic systems in the offshore industry. Energies 2021;14. https://doi.org/10.3390/en14216988.

[4] Claus R, López M. Key issues in the design of floating photovoltaic structures for the marine environment. Renew Sustain Energy Rev 2022;164:112502. https://doi.org/10.1016/j.rser.2022.112502.

[5] Maia A, Ferreira E, Oliveira MC, Menezes LF, Andrade-Campos A. 3 - Numerical optimization strategies for springback compensation in sheet metal forming. In: Paulo Davim J, editor. Comput Meth Prod Eng. Woodhead Publishing; 2017. p. 51–82.

[6] Marciniak Z, Duncan JL, Hu SJ. Mechanics of Sheet Metal Forming. Oxford: Butterworth-Heinemann; 2002.

[7] Schijve J. Fatigue of structures and materials in the 20th century and the state of the art. Int J Fat 2003;25:679–702. https://doi.org/10.1016/S0142-1123(03)00051-3.

[8] Haagensen PJ, Larsen JE, Vårdal OT. Fatigue damage repair and life extension of a floating production unit: the VFB Platform revisited. : ASME 2011 30th Int Conf Ocean Offshore Arct Eng 2011:649–62.

[9] Hallquist J. Preliminary user's manuals for DYNA3D and DYNAP (Nonlinear dynamic analysis of solids in three dimensions). California: Livermore. 1976. https://doi.org/10.2172/7349375.

[10] Hallquist J.O., Benson D.J. DYNA3D user's manual (nonlinear dynamic analysis of structures in three dimensions). 1987. ⟨https://www.osti.gov/biblio/6157492⟩ (accessed April 2, 2024).

[11] Banabic D, Barlat F, Cazacu O, Kuwabara T. Advances in anisotropy of plastic behaviour and formability of sheet metals. Int Mat Form 2020;13:749–87. https://doi.org/10.1007/s12289-020-01580-x.

[12] El Sherbiny M, Zein H, Abd-Rabou M, El shazly M. Thinning and residual stresses of sheet metal in the deep drawing process. Mat Des 2014;55:869–79. https://doi.org/10.1016/j.matdes.2013.10.055.

[13] Zein H, El Sherbiny M, Abd-Rabou M, El shazly M. Thinning and spring back prediction of sheet metal in the deep drawing process. Mat Des 2014;53:797–808. https://doi.org/10.1016/j.matdes.2013.07.078.

[14] Hariharan K, Prakash RV, Sathya Prasad M. Influence of yield criteria in the prediction of strain distribution and residual stress distribution in sheet metal formability analysis for a commercial steel. Mat Manuf Process 2010;25:828–36. https://doi.org/10.1080/10426910903496847.

[15] Hariharan K, Prakash RV, Sathya Prasad M, Madhusudhan Reddy G. Evaluation of yield criteria for forming simulations based on residual stress measurement. Int J Mat Form 2010;3:291–7. https://doi.org/10.1007/s12289-010-0984-9.

[16] Tang B, Lu X, Wang Z, Zhao Z. Springback investigation of anisotropic aluminum alloy sheet with a mixed hardening rule and Barlat yield criteria in sheet metal forming. Mat Des 2010;31:2043–50. https://doi.org/10.1016/j.matdes.2009.10.017.

[17] Mulidrán P, Šiser M, Slota J, Spišák E, Sleziak T. Numerical prediction of forming car body parts with emphasis on springback. Metals 2018;8:435. https://doi.org/10.3390/met8060435.

[18] Yoon JW, Hong SH. Modeling of aluminum alloy sheets based on new anisotropic yield functions. J Mat Process Tech 2006;177:134–7. https://doi.org/10.1016/j.jmatprotec.2006.03.189.

[19] Zhang X, Ma Ye, Li W, Huang W, Zhang W, Wang Z. A review of residual stress effects on fatigue properties of friction stir welds. Criti Rev Solid State Mat Sci 2023;48:775–813. https://doi.org/10.1080/10408436.2022.2138828.

[20] Abdelbaset H, Zhu Z. Behavior and fatigue life assessment of orthotropic steel decks: a state-of-the-art-review. Structures 2024;60:105957. https://doi.org/10.1016/j.istruc.2024.105957.

[21] Facchinetti ML, Weber B, Doudard C, Calloch S. Taking into account the forming process in fatigue design computations. : Fat Des 2007: Recl Des Conf Proc 2008.

[22] Dang-Van K. Macro-Micro Approach in High-Cycle Multiaxial Fatigue. ASTM Int. 1993. https://doi.org/10.1520/STP24799S.

[23] Dannbauer H, Gaier C, Aichberger W. Integrating the results from process simulation into fatigue life prediction. SAE Techn Pap No-2007-26-071. Soc Automot Eng, Warrendale, PA, USA 2007:1–6. https://doi.org/10.4271/2007-26-071.

[24] Kose KR, B. Plasticity effects in subsequent simulations of car structures, In: 7th Int Conf Comput Plast, COMPLAS 2003. Barcelona, Spain; 2003.

[25] Hariharan K, Prakash RV. Integrating effect of forming in fatigue life prediction: review of present scenario and challenges. Proc Inst Mech Eng Part B-J Eng Manuf 2012;226:967–79. https://doi.org/10.1177/0954405412437621.

[26] Dassault Systèmes. Abaqus analysis user's manual. 2007.

[27] Masendorf R. Einfluss der Umformung auf die zyklischen Werkstoffkennwerte von Feinblech. Papierflieger; 2000.

[28] Galtier A, Philippe C, MARONNE E, Yoshida Y, Atsushi S, ROBERT J-L. Integration of process operation in the fatigue calculation of sheets structural parts. SAE Tech Pap 2003. https://doi.org/10.4271/2003-01-2879.

[29] Sines G, Ohgi G. Fatigue criteria under combined stresses or strains. J Eng Mat Tech 1981;103:82–90. https://doi.org/10.1115/1.3224995.

[30] Voce E. The relationship between stress and strain for homogeneous deformation. J Inst Met 1948:74.

[31] Livermore Software Technology Corporation. LS-DYNA® Theory Manual. 2019.

[32] Barlat F, Brem JC, Yoon JW, Chung K, Dick RE, Lege DJ, et al. Plane stress yield function for aluminum alloy sheets - part 1: theory. Int J Plast 2003;19:1297–319. https://doi.org/10.1016/S0749-6419(02)00019-0.

[33] Hershey AV. The elasticity of an isotropic aggregate of anisotropic cubic crystals. J Appl Mech 1954;21:236–40. https://doi.org/10.1115/1.4010899.

[34] Logan RW, Hosford WF. Upper-bound anisotropic yield locus calculations assuming ⟨111⟩-pencil glide. Int J Mech Sci 1980;22:419–30. https://doi.org/10.1016/0020-7403(80)90011-9.

[35] Barlat F, Aretz H, Yoon JW, Karabin ME, Brem JC, Dick RE. Linear transfomation-based anisotropic yield functions. Int J Plast 2005;21:1009–39. https://doi.org/10.1016/j.ijplas.2004.06.004.

[36] Aretz H, Barlat F. New convex yield functions for orthotropic metal plasticity. Int J Nonlin Mech 2013;51:97–111. https://doi.org/10.1016/j.ijnonlinmec.2012.12.007.

[37] Lademo OG, Hopperstad OS, Langseth M. An evaluation of yield criteria and flow rules for aluminium alloys. Int J Plast 1999;15:191–208. https://doi.org/10.1016/S0749-6419(98)00064-3.

[38] Gruben G, Sølvernes S, Berstad T, Morin D, Hopperstad OS, Langseth M. Low-velocity impact behaviour and failure of stiffened steel plates. Mar Struct 2017;54:73–91. https://doi.org/10.1016/j.marstruc.2017.03.005.

[39] Morin D, Kaarstad BL, Skajaa B, Hopperstad OS, Langseth M. Testing and modelling of stiffened aluminium panels subjected to quasi-static and low-velocity impact loading. Int J Impact Eng 2017;110:97–111. https://doi.org/10.1016/j.ijimpeng.2017.03.002.

[40] Espeseth V, Børvik T, Hopperstad OS. Aluminium plates with geometrical defects subjected to low-velocity impact: Experiments and simulations. Int J Impact Eng 2022;167:104261. https://doi.org/10.1016/j.ijimpeng.2022.104261.

[41] Granum H, Morin D, Børvik T, Hopperstad OS. Calibration of the modified Mohr-Coulomb fracture model by use of localization analyses for three tempers of an AA6016 aluminium alloy. Int J Mech Sci 2021;192:106122. https://doi.org/10.1016/j.ijmecsci.2020.106122.

[42] La.Vision GmbH. 2D-/3D Stereo DIC. https://lavision.de/en/products/strainmaster/2d-stereo-dic/index.php (Accessed 2 April 2024).

[43] Dick RE, Yoon JW. Plastic anisotropy and failure in thin metal: Material characterization and fracture prediction with an advanced constitutive model and polar EPS (effective plastic strain) fracture diagram for AA 3014-H19. Int J Solid Struct 2018;151:195–213. https://doi.org/10.1016/j.ijsolstr.2018.03.008.

[44] Anderson N, Brown D, McMurray RJ, Leacock AG. The influence of uniaxial prestrain on biaxial r-values in 7075-O aluminium alloy. AIP Conf Proc 2011;1353:1435–40. ⟨https://doi.org/10.1063/1.3589718⟩.

[45] Vysochinskiy D. Formability of aluminium alloy subjected to prestrain by rolling. 2014.

[46] Rizzi E, Hähner P. On the Portevin–Le Chatelier effect: theoretical modeling and numerical results. Int J Plast 2004;20:121–65. https://doi.org/10.1016/S0749-6419(03)00035-4.

[47] Clausen AH, Børvik T, Hopperstad OS, Benallal A. Flow and fracture characteristics of aluminium alloy AA5083–H116 as function of strain rate, temperature and triaxiality. Mat Sci Eng: A 2004;364:260–72. https://doi.org/10.1016/j.msea.2003.08.027.

[48] Benallal A, Berstad T, Børvik T, Hopperstad O, Koutiri I, De Codes RN. An experimental and numerical investigation of the behaviour of AA5083 aluminium alloy in presence of the Portevin–Le Chatelier effect. 45 Int J Plast 2008;24:1916. https://doi.org/10.1016/j.ijplas.2008.03.008.

[49] Tian N, Wang G, Zhou Y, Liu K, Zhao G, Zuo L. Study of the Portevin-Le Chatelier (PLC) characteristics of a 5083 aluminum alloy sheet in two heat treatment states. Materials 2018;11:1533. https://doi.org/10.3390/ma11091533.

[50] Vysotskii I, Malopheyev S, Mironov S, Kaibyshev R. Effect of elastic stress on diffusion-assisted phenomena in an Zr-modified 5083 aluminum alloy. J Alloy Compd 2023. https://doi.org/10.1016/j.jallcom.2023.169897.

[51] MATLAB Version 9.10. 0.1602886 (R2021a). 2021.

[52] Belytschko T, Lin JI, Chen-Shyh T. Explicit algorithms for the nonlinear dynamics of shells. Comput Methods Appl Mech Eng 1984;42:225–51. https://doi.org/10.1016/0045-7825(84)90026-4.

[53] Wang WR, Chen GL, Lin ZQ. The study on the fatigue FEM analysis considering the effect of stamping. Mat Des 2009;30:1588–94. https://doi.org/10.1016/j.matdes.2008.07.046.
[54] Sines G. Failure of materials under combined repeated stresses with superimposed static stresses. 1955.
[55] Ottosen NS, Stenstrom R, Ristinmaa M. Continuum approach to high-cycle fatigue modeling. Int J Fat 2008;30:996–1006. https://doi.org/10.1016/j.ijfatigue.2007.08.009.
[56] Lindstrom SB. Continuous-time, high-cycle fatigue model for nonproportional stress with validation for 7075-T6 aluminum alloy. Int J Fat 2020;140. https://doi.org/10.1016/j.ijfatigue.2020.105839.
[57] Sidhom N, Laamouri A, Fathallah R, Braham C, Lieurade HP. Fatigue strength improvement of 5083 H11 Al-alloy T-welded joints by shot peening: experimental characterization and predictive approach. Int J Fat 2005;27:729–45. https://doi.org/10.1016/j.ijfatigue.2005.02.001.
[58] Tveit S, Reyes A, Erduran E. Forming effects on high-cycle fatigue in an aluminum sheet structure using the Ottosen-Stenström-Ristinmaa model. : 8th Eur Congr Comput Method Appl Sci Eng 2022.